sustainability

Article

A Numerical-Hierarchical Framework for Predicting Volume Changes in Expansive Soils under Variable Surface and Weather Conditions

Qihang Huang and Shahid Azam *

Environmental Systems Engineering, Faculty of Engineering and Applied Science, University of Regina, 3737 Wascana Parkway, Regina, SK S4S 0A2, Canada
* Correspondence: shahid.azam@uregina.ca

Abstract: This research developed a numerical-hierarchical framework that captured surface conditions and climate parameters. Volume changes under distinct scenarios of surface boundary, antecedent moisture, and meteorological parameters were predicted using a coupled seepage-deformation model. Risk was hierarchically based on expert judgment for surface scenarios (Stage-I indices) and normal distribution for antecedent moisture and atmospheric parameters scenarios (Stage-II indices). Results indicated seasonal volumetric changes with minor variations of −5 mm from January to April, a steady settlement of −17 mm by June, and a gradual heave of +8 mm by December. All Stage-I indices showed similar trends such that the fluctuations were highest for vegetation, followed by slope, then by cover, and lowest for loading. Volume changes gradually reduced with depth and diminished at 3.1 m. Similar seasonal and profile trends were generally found for most Stage-II indices. Nonetheless, different trends under wet and dry conditions were observed for initial water content, precipitation, and air temperature. For the datum scenario, risk was non-existent till February, increased to 2.3 by June, diminished by October, and rose back to 1.0 by December. Similar values of cyclic variations in risk were found in most urban facilities. Volume changes were found to be two times higher in parks, insignificant for roads, half for five story buildings, and one-fourth for pipes under roads. Among the Stage-II indices, risk for the initial water content inhibited seasonal variations whereas that for precipitation was about half with a wider distribution; all the other indices showed about one-third the values. Under a higher occurrence probability of 0.129, a magnified risk was observed for all the indices such that the most critical were the initial water content and precipitation.

Keywords: risk assessment; numerical model; hierarchical approach; volumetric changes; expansive soil; surface conditions; seasonal weather

check for updates

Citation: Huang, Q.; Azam, S. A Numerical-Hierarchical Framework for Predicting Volume Changes in Expansive Soils under Variable Surface and Weather Conditions. *Sustainability* **2023**, *15*, 4200. https://doi.org/10.3390/su15054200

Academic Editor: Iason Verginelli

Received: 27 January 2023
Revised: 23 February 2023
Accepted: 24 February 2023
Published: 26 February 2023

1. Introduction

Expansive soils are widely distributed in arid and semiarid regions of the globe. Countries or regions such as Australia [1], Canada [2], China [3], India [4], the Middle East [5], and the United States [6] have suffered from damage that originated from swell and shrink of such soils. The swell and shrink behavior of this soil is a response of positive charged water entering the negative clay mineral layer, which exhibits swelling when wetted and shrinkage when dried [7]. Weather is the main contributor for expansive soil swell and shrink and directly governs the potential damages from such soil [8]. The potential damage from clay includes road crack [9], house movement [10], and pipe leakage [11]. Detailed damage data includes 19 km of damaged road, costing $11 million in 2017 in the City of Regina [12]; annual damage in residential and commercial buildings of Sudan reported to exceed $6 million [13]; and the predicted annual loss related to expansive soil damage totaling $30 billion in the United States and China [14]. A comparable cost should be expected for hazards due to similar soils in the Canadian Prairies, owing to the extreme climatic conditions and seasonal weather variations prevalent in the region.

Given the potential damage of expansive soils, there is a need to conduct risk assessment. Existing methods include probabilistic models [15]; multi-criteria evaluation (MCE) [16]; multi-criteria decision analysis (MCDA) [17,18]; and the analytic hierarchy process (AHP) [19–21]. The widely used AHP method is a multi-criteria decision-making approach in which factors are arranged in a hierarchic structure [22]. The magnitude and possibility of different evaluation indices are collected and used in constructing a fuzzy decision matrix. The application of the AHP method to volumetric changes in expansive soils can be divided on the basis of the required evaluation indices and the resulting outputs, as follows: (a) those based on a single index of soil properties, including clay content, consistency limit, and soil mineralogy [19]; and (b) those based on multiple indices of soil properties and variation of water content [20,21]. In the first type, only a range of heave and settlement is computed, and as a result, no consideration is given to flow though and volume change arising from metrological parameters. Although this is easy to carry out, it cannot capture transient analysis. In the second type, transient volume changes can be included only when extensive field monitoring data are available and the soil surface is open to interact with the atmosphere. Therefore, a numerical-hierarchical framework is required to capture variations in both surface conditions and seasonal weather.

The main objective of this research was to develop a numerical-hierarchical framework for predicting volume changes in expansive soils under variable surface and weather conditions. Based on published soil properties, various surface conditions, antecedent moistures, and metrological parameters were used to develop distinct scenarios using a coupled seepage-deformation model [23]. The various scenarios were hierarchically analyzed to determine the risk evaluation vector based on expert judgment and normal distribution.

2. Theoretical Background

Figure 1 gives the theoretical background of the AHP method of risk assessment [24–26]. The figure shows the three main components of risk assessment, including the following [27]: risk identification (finding, recognizing, and describing), risk analysis (understanding the nature and calculating the level of risk), and risk evaluation (comparing the results with criteria).

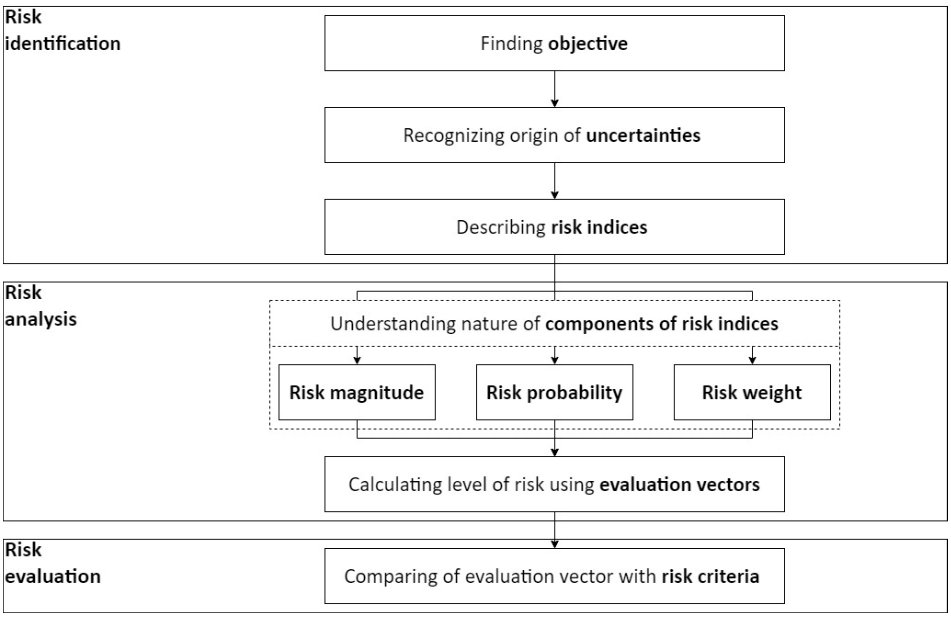

Figure 1. Theoretical background of hierarchical risk assessment model.

Risk identification involves finding the objective (benchmark for the expected result), recognizing the origin of the uncertainties (deficient information of an event), and describing the uncertainties using the risk indices (event categories with potential impacts on objective results) [28]. The problem is structured as a hierarchy by treating the various risk indices in stages [22]. The Stage-I indices are related to the objective but may not be quantifiable and, as such, are required to be scaled based on experience. The Stage-II indices are related to the Stage-I indices, and since they are quantifiable, these contribute to the final goal in a stepwise manner [29]. Each risk index is analyzed by understanding the following components: (i) magnitude (consequence on the objective); (ii) probability (likelihood of occurrence), and (iii) weight (relative significance). These components are combined using the matrix evaluation vector (Q) to quantify the level of risk.

The evaluation vector at Stage-II indices (B) is calculated based on Equation (1), and the overall evaluation vector (Q) is calculated by combining the Stage-I and the Stage-II indices in Equation (2), as given below:

$$B = \sum_{i=1}^{n} s_{ti} \sum_{t=1}^{m} v_{ti} \cdot p_{ti} = \begin{bmatrix} s_{11} & \cdots & s_{m1} \\ \cdots & \cdots & \cdots \\ s_{1n} & \cdots & s_{mn} \end{bmatrix} \begin{bmatrix} v_{11} \cdot p_{11} & \cdots & v_{1n} \cdot p_{1n} \\ \cdots & \cdots & \cdots \\ v_{m1} \cdot p_{m1} & \cdots & v_{mn} \cdot p_{mn} \end{bmatrix} = \begin{bmatrix} b_{11} & \cdots & b_{1n} \\ \cdots & \cdots & \cdots \\ b_{m1} & \cdots & b_{mn} \end{bmatrix} \quad (1)$$

In the above equation, s_{ti} is the weight of an index with the rank (i = 1, 2, . . . , m) and the associated risk factor (t = 1, 2, . . . , n); v_{ti} is the magnitude of an index with rank i and risk factor t; and p_{ti} is the probability of an index i and factor t.

$$Q = \sum_{r=1}^{o} w_r B = \begin{bmatrix} w_1 \\ \cdots \\ w_o \end{bmatrix} \begin{bmatrix} b_{11} & \cdots & b_{1\mathrm{n}} \\ \cdots & \cdots & \cdots \\ b_{m1} & \cdots & b_{no} \end{bmatrix} \quad (2)$$

In the above equation, w_r is the weight of Stage-I indices, and r is the number of Stage-I indices (r = 1, 2, ..., O).

Risk evaluation is the process of comparing the evaluation vector (Q) with the risk criteria (the evaluation tool works as term of reference against analysis tool) to accept or reject the results. The risk criteria are defined as the terms of reference, which are derived from standards, bylaws, policies, industry specifications, or based on the default datum.

3. Research Methodology

Figure 2 gives the flow chart of the risk modeling process. The objective was defined as the volumetric change of soil in the vertical direction. The uncertainties included four distinct event categories: soil properties, surface conditions, initial water content, and meteorological parameters. These uncertainties were described by Stage-I indices with a non-quantifiable effect on the objective and Stage-II indices having quantifiable effect on the objective.

Soil properties (Figure 3) comprised index properties (specific gravity = 2.75 and plastic limit = 28%), water retention curve (WRC), hydraulic conductivity curve (HCC), and swell shrink curve (SSC) [30]. These indices were assumed to be constant because of the largely homogenous nature of the soil deposit [31]. Likewise, various surface conditions included cover, loading, slope, and vegetation of the underlying soil. These variable indices were subsequently assigned to different infrastructure types using expert judgment. Constant soil properties and the use of expert judgement ensured that the Stage-I indices have a quantifiable effect on the objective. In contrast, the Stage-II indices included the initial water content obtained from the field water content profile [30] and meteorological parameters (precipitation, temperature, humidity, wind, and radiation) analyzed using daily data from 1970 to 2015. The effect of these variable risk indices was quantifiable.

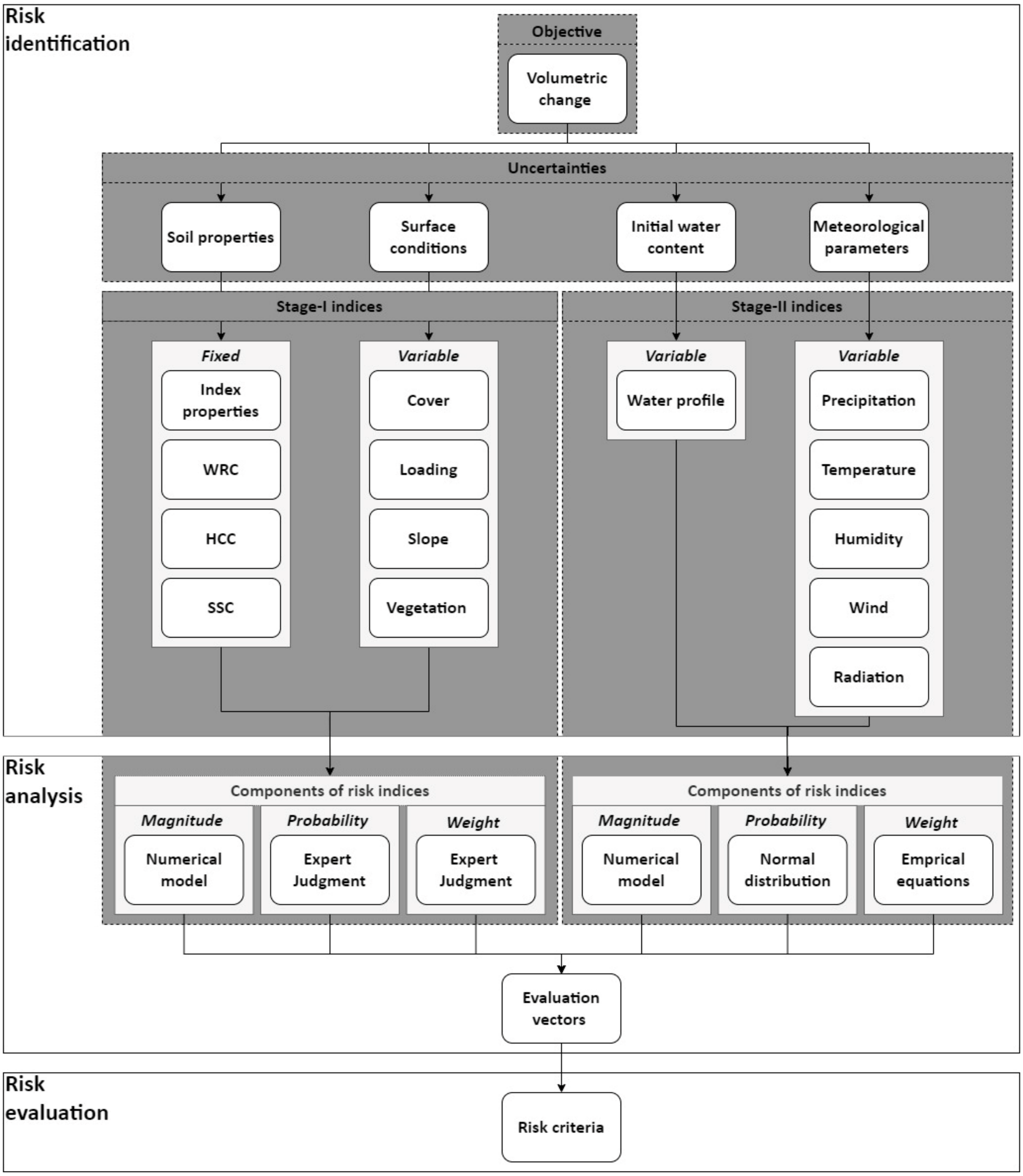

Figure 2. Layout of the numerical-hierarchical framework.

Various data preparation methods were used to determine the components of risk indices (magnitude, probability, and weight). The magnitude (v) of all risk indices was predicted through a coupled numerical model comprising soil–atmosphere interactions using a commercial software (GeoStudio 2020) and volume change predictions based on empirical equations [30]. A homogeneous soil column was modeled up to 3.2 m depth and was divided along the profile into 16 layers of 0.2 m thickness. The initial conditions included soil properties and initial water contents, whereas the boundary conditions comprised surface conditions and meteorological parameters. Soil temperature and snow cover depth were calculated based on meteorological parameters and applied to the model as boundary conditions. Further details about model development and validation were provided earlier [23].

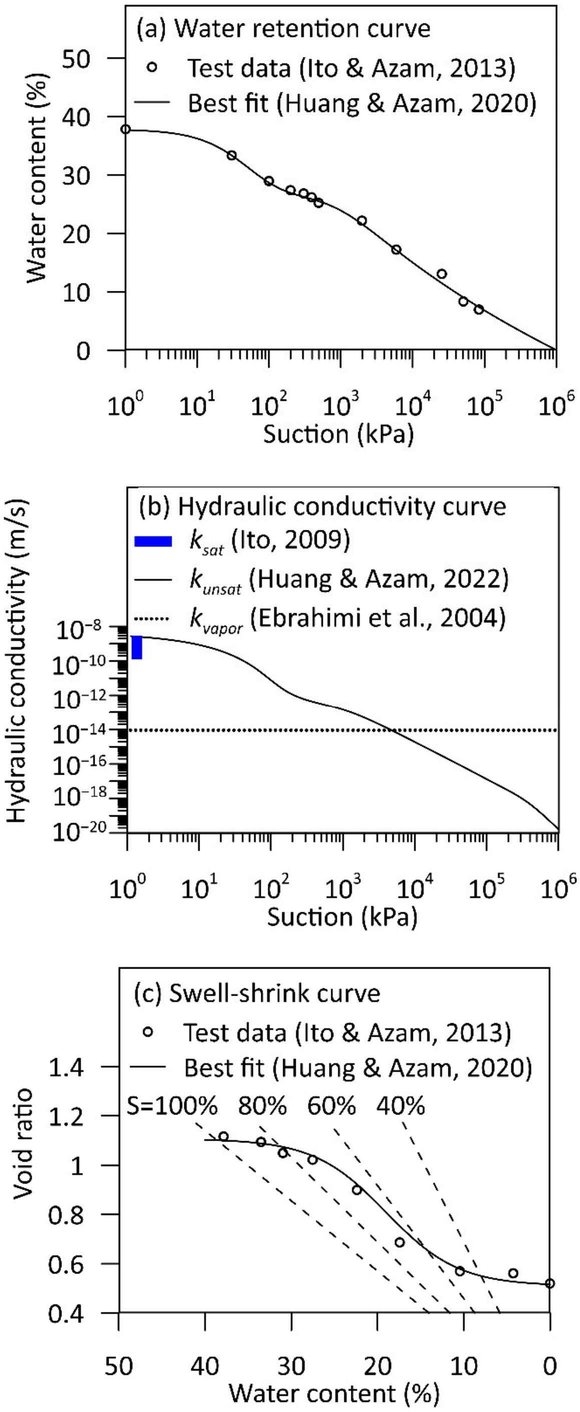

Figure 3. Soil behavior functions: (**a**) water retention curve; (**b**) hydraulic conductivity curve; and (**c**) swell-shrink curve [23,30,32–34].

The datum scenario had an upper boundary of no cover, no loading, no slope, and no vegetation along with mean values of meteorological parameters; the mean initial water content was applied to the entire soil column. A probability of 12.9% (pertaining to ±0.3 standard deviation) was set to assume no variations of all indices within this range.

The probability (p) of Stage-I indices was defined as the ratio of area under a given soil condition divided by the total area. Using constant soil properties, seventeen scenarios were modeled. Four surface scenarios used maximum conditions one at a time while keeping all other indices the same as the datum scenario. The maximum conditions were cover (of 0.15 m thick asphalt with a hydraulic conductivity of 3×10^{-7} m/s [35,36]), loading (allowable design stress of 300 kPa for expansive soils [37]), slope (assumed gradient of 45° with the horizontal), and vegetation (root zone depth of 0.35 m [38]). The probability of these variables was set to be 100% to provide equal chance of occurrence.

The probability of Stage-II indices was calculated using normal distribution function (NDF). Two initial water content scenarios were modeled using the dry and the wet profiles (Figure 4) one at a time while keeping all other indices the same as the datum scenario; the climate-dependent parameters of snow depth and soil temperature were also kept at the datum. The 2-year field measurements [30] for initial water content were analyzed in 1 m layers to obtain mean values. The standard deviation was calculated to obtain the 95% confidence interval for each layer. Therefore, the probability of extreme water content was set as 2.5%. Finally, ten extreme scenarios (Figure 5) were modeled using the highest and lowest values of each metrological parameter one at a time while keeping all other indices the same as datum. The climate-dependent parameters were assigned based on the corresponding Stage-II indices, for example, dry snow depth for dry precipitation and so on. The 45-year daily data of atmospheric parameters (precipitation, air temperature, relative humidity, wind speed, and net radiation) were statistically analyzed to obtain daily mean values and 95% confidence interval for each parameter. Again, the probability of extreme meteorological parameters was set as 0.5% and pertained to a 40-year return period.

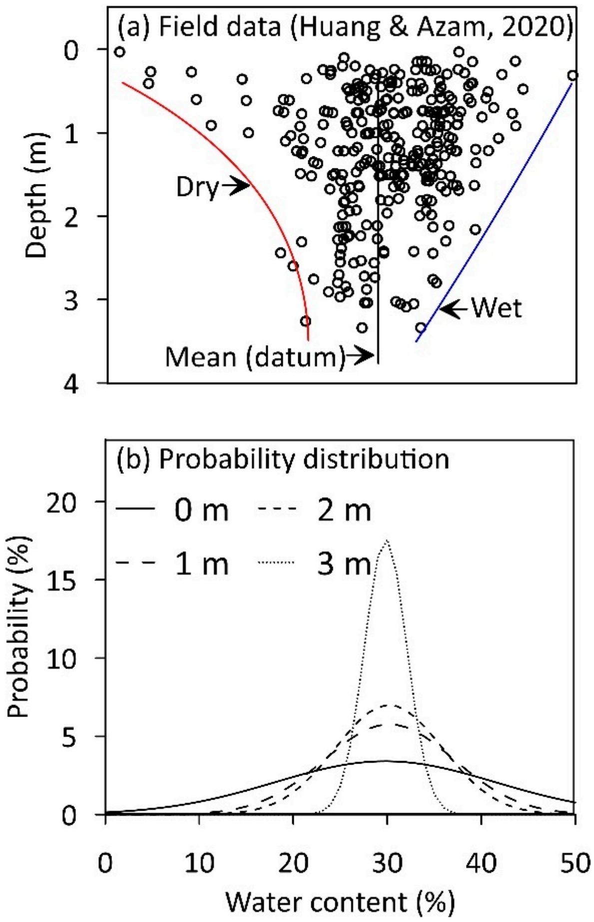

Figure 4. Analysis of initial water content: (**a**) field data and (**b**) normal distribution functions at selected depths [30].

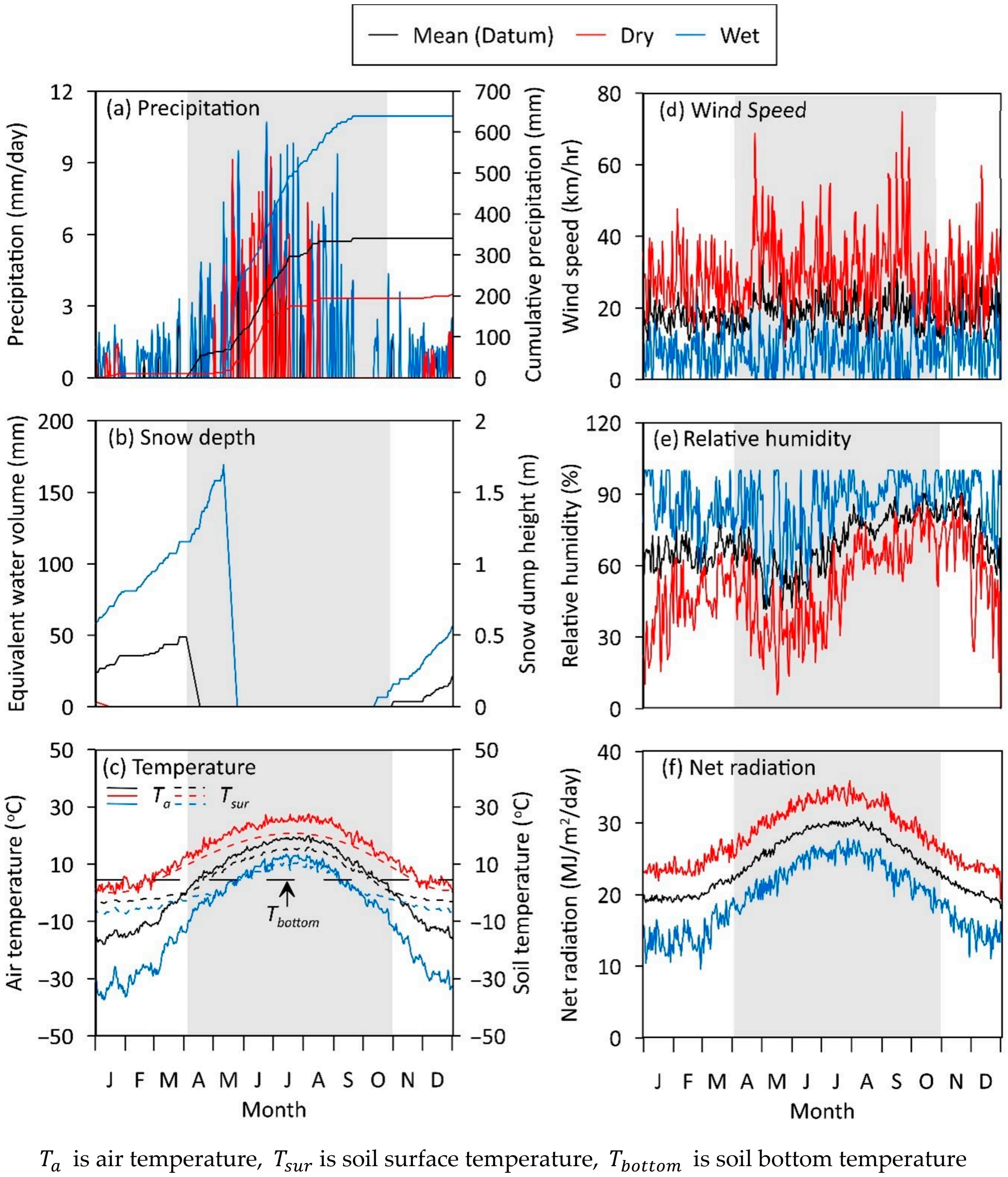

Figure 5. Simulated meteorological parameters for the investigated area: (**a**) precipitation; (**b**) snow depth; (**c**) temperature; (**d**) wind speed; (**e**) relative humidity; and (**f**) net radiation.

The overall weight (w_r) of Stage-I indices (r) (Table 1) was calculated for eight selected infrastructure types. Based on expert judgement, an area factor (A_r, percentage of area affected by a given index) and a scaling factor (L_r, linear interpolation between datum and maximum of a given index) were assigned. The following equation was used to determine the overall weight:

$$w_r = \frac{A_r L_r}{\sum_{r=1}^{4} A_r L_r} \tag{3}$$

In contrast, the weight of Stage-II risk indices was set to be 1 because the influence of each parameter was included in the governing equation of the coupled model [23]. The evaluation vector (Q) of each risk index was calculated separately for Stage-I and Stage-II indices using Equations (1) and (2), respectively. The risk was evaluated by comparing Q for each index using the risk criteria, that is, the datum model.

Table 1. Summary of Stage-I risk indices for the investigated urban infrastructure.

Facility Type	Index	Area Factor (A_r)	Scaling Factor (L_r)	Overall Weight (W_r)	Rationale and Reference
Park	Cover	0	0	0	No construction
	Loading	0	0	0	No construction
	Slope	1	0.1	0.1	Low average slope of 0.5° (100:1) with marginal runoff [39]
	Vegetation	1	1	0.9	High average root depth of 0.35 m for grass and trees with full evapotranspiration [38]
Parking Lot	Cover	1	1	0.8	Average asphalt thickness of 0.15 m with full insulation from atmosphere per Bylaw 2325 [36]
	Loading	0	0	0	Vehicular load not considered
	Slope	1	0.2	0.2	Medium average slope of 8.3° (12:1) with moderate runoff per Bylaw 2999 [40]
	Vegetation	0	0	0	Flowerbeds not considered
Unpaved Road	Cover	0.8	0.5	0.55	Average gravel thickness of 0.15 m with partial insulation from atmosphere per Bylaw 2120 [41]
	Loading	0	0	0	Vehicular load not considered
	Slope	1	0.2	0.3	Medium average slope of 8.3° (12:1) with moderate runoff per Bylaw 2999 [40]
	Vegetation	0.2	0.6	0.15	Medium average root depth of 0.2 m for grass with moderate evapotranspiration on shoulders [42]
Paved Road	Cover	1	1	0.7	Average asphalt thickness of 0.15 m with full insulation from atmosphere per Bylaw 2325 [36]
	Loading	0	0	0	Vehicular load not considered
	Slope	1	0.4	0.3	High average slope of 18.5° (3:1) with high runoff [43]
	Vegetation	0	0	0	No vegetation on shoulders
Single Storey House	Cover	0.2	1	0.3	Average asphalt thickness of 0.15 m with full insulation from atmosphere per Bylaw 2325 [36]
	Loading	0.6	0.2	0.4	60 kPa distributed over strip footing [44]
	Slope	1	0	0	Prepared as flat compacted ground with roof runoff collected by storm sewer
	Vegetation	0.2	1	0.3	High average root depth of 0.35 m for grass/trees with full evapotranspiration in lawns [38]
Five Storey Building	Cover	0.4	1	0.4	Average asphalt thickness of 0.15 m with full insulation from atmosphere per Bylaw 2325 [36]
	Loading	0.6	1	0.6	300 kPa for five floors mat footing [44]
	Slope	1	0	0	Prepared as flat compacted ground with roof runoff collected by storm sewer
	Vegetation	0	0	0	No vegetation due to plinth protection
Pipe in Back Alley	Cover	0.8	0.5	0.55	Average gravel thickness of 0.15 m with partial insulation from atmosphere per Bylaw 2120 [41]
	Loading	0	0	0	Soil overburden considered with respect to depth
	Slope	1	0.2	0.3	Medium average slope of 8.3° (12:1) with moderate runoff per Bylaw 2999 [40]
	Vegetation	0.2	0.6	0.15	Medium average root depth of 0.2 m for grass with moderate evapotranspiration on shoulders [42]
Pipe in Front Road	Cover	1	1	0.7	Average asphalt thickness of 0.15 m with full insulation from atmosphere per Bylaw 2325 [36]
	Loading	0	0	0	Soil overburden considered with respect to depth
	Slope	1	0.4	0.3	High average slope of 18.5° (3:1) with high runoff [43]
	Vegetation	0	0	0	No vegetation on shoulders

4. Data Preparation

Figure 3 presents the soil behavior functions for the investigated soil. The shapes of these functions are attributed to soil fabric that comprises discontinuous cracks as well as a soil matrix of particles and pores. Derived from spatially variable deformations and geological stress history, cracks are found in both natural deposits [32] and compacted soils [45]. The cracks periodically open during shrinkage (drying due to evaporation) and close during swelling (wetting due to precipitation). The WRC (Figure 3a) shows two air entry values, with the first (8 kPa) for air entering the soil cracks and the second (300 kPa) for air entering the soil matrix. Likewise, there are two residual values, with the first (100 kPa) pertaining to water leaving the crack walls and the second (2×10^4 kPa) corresponding to adsorbed water removal from the soil particles. The saturated hydraulic conductivity (ksat) was reported to range from 5×10^{-9} m/s to 10^{-10} m/s [33]. Starting at the highest value, the HCC (Figure 3b) showed a marginal reduction up to 1×10^{-9} m/s at 8 kPa. Thereafter, the unsaturated value (kunsat) decreased drastically to 1×10^{-12} m/s at the second air entry of 300 kPa, to 5×10^{-16} m/s at the second residual suction of 2×10^4 kPa, and to 1×10^{-20} m/s under completely dry conditions. In contrast, vapor conductivity (kvapor) remained at 1×10^{-14} m/s and met the HCC around 3000 kPa [34]. Finally, the SSC (Figure 3c) comprised a low structural shrinkage (with e reduced from 1.1 to 1.0) where water flows through cracks, a high normal shrinkage (with e reduced from 1.0 to 0.6) where water flows through the soil matrix, and a low residual shrinkage (with e reduced from 0.5 to 0.6) where water leaves particle surfaces [23].

Figure 4 shows the analysis of the initial water content data. The water content profile (Figure 4a) showed a funnel-shaped trend with a mean water content of 28% and a range of 5% to 45% at the surface that tended to reach 28% at 3.5 m depth. As mentioned earlier, the various scenarios were defined based on the 95% confidence interval using NDA (Figure 4b). Generally, these curves were found to be bell-shaped and were centered at 28%, which pertains to the plastic limit of the soil. Using σ for standard deviation, w_c for measured water content, and μ for arithmetic mean, probability curves were developed following NDA [46]:

$$f(x) = \frac{1}{\sqrt{2\pi\sigma^2}} e^{\frac{(w_c-\mu)^2}{2\sigma^2}} \tag{4}$$

Figure 5 presents the simulated meteorological parameters of mean (datum), dry, and wet years for the investigated area. These daily average values were retrieved from Environment Canada at the Regina International Airport station (ID 4016560) for precipitation, air temperature, relative humidity, and wind speed and the Power NASA database (Access Viewer) for net radiation. The cumulative snow depth was calculated by adding daily precipitation values when air temperature (T_a, °C) was below zero and assuming snow density remained at 100 kg/m^3 [47]. When the air temperature was above 0 °C, a daily water volume corresponding to snowmelt was applied at a constant rate over a two-week period [31]. Furthermore, the soil surface temperature (T_{sur}, °C) was calculated for no-snow-cover days according to the following equation [48]:

$$T_{sur} = T_a + \frac{Q_n - AE}{0.35\eta(1 + 0.146W_w)} \tag{5}$$

In the above equation, Q_n is net radiation (mm/day), AE is actual evaporation (mm/day) obtained using GeoStudio 2020, η is psychrometric constant (0.06733 kPa/°C), 0.35 (1 + 0.146 Ww) (mm/day/kPa) is an empirical expression for turbulent exchange (Penman, 1948) including W_w as wind speed (km/hr). Likewise, the soil surface temperature under snow cover was assumed to be 20% of T_a. The bottom soil temperature at 3.2 m was fixed at 4.6 °C, based on measured data in Regina [49]. The seasons were defined on the basis of mean air temperature, that is, winter (November to March) was below 0 °C and summer (April to October) was above 0 °C.

The mean data (datum) shows 92 days of precipitation, with a cumulative value of 341 mm comprising 49 mm snowmelt (0.49 m of snow depth) and 292 mm rain. The snow depth was allowed to melt at a rate of 3.5 mm/day from 4 to 17 April. The average values for the remaining parameters were found to be as follows: air temperature, −10 °C in winter and 12 °C in summer; soil surface temperature, −2 °C in winter and 9.5 °C in summer; wind speed, 18 km/h in both seasons; relative humidity, 70% in both seasons; and net radiation, 20 MJ/m^2/day in winter to 30 MJ/m^2/day in summer. This mean weather is classified as Dfb according to the Köppen climate classification.

The dry scenarios (obtained from the same database sources) include lowest precipitation, highest temperature, lowest humidity, highest wind, and highest radiation; these values were derived from daily data over the 45-year period. The dry scenario shows 49 days of precipitation, with a cumulative value of 203 mm comprising 3 mm snowmelt (0.03 m snow) and 200 mm rain. The snow depth was allowed to melt at a rate of 0.24 mm/day from 3 to 17 January. The average values for the remaining parameters were as follows: air temperature, 2 °C in winter and 21 °C in summer; soil surface temperature, −3 °C in winter and 17 °C in summer; wind speed, 28 km/h in winter and 31 km/h in summer; relative humidity, 50% for both seasons; and net radiation, 24 MJ/m^2/day in winter and 37 MJ/m^2/day in summer. The dry scenarios simulated drought with a 40-year return period for each of the atmospheric parameters. Similar dry weather spells occurred in 1984 with 225 mm precipitation and in 2017 with 157 mm precipitation [39].

The wet scenarios (obtained from the same database sources) include highest precipitation, lowest temperature, highest humidity, lowest wind, and lowest radiation; these values were derived from daily data over the 45-year period. The wet scenario shows 181 days of precipitation, with a cumulative value of 639 mm comprising 169 mm snowmelt (1.69 m of snow depth) and 470 mm rain. The snow cover was allowed to melt at a rate of 12.1 mm/day from 12 to 25 May. The rest of the parameters registered the following average values: air temperature, −27 °C in winter and 3 °C in summer; soil surface temperature, −5.1 °C in winter and 3.8 °C in summer; wind speed, 7 km/h in both seasons; relative humidity, 86% for both seasons; and net radiation, 14 MJ/m^2/day in winter and 23 MJ/m^2/day in summer. The wet scenarios pertained to a 40-year return period for each of the atmospheric parameters. Similar wet weather conditions prevailed during 2010 with 576 mm precipitation and 2014 with 502 mm precipitation [39].

5. Results and Discussion

Figure 6 gives predicted net water flux for the mean, dry, and wet scenarios. Under the mean scenario (Figure 6a), the daily flux remained constant during winter due to snow cover and frozen surface and was followed by a variation of ±10 mm/day during summer due to alternate rainfall and evaporation. In contrast, the dry scenario (Figure 6b) shows up to −5 to +2 mm/day (higher than mean scenario) because of lack of snow and frozen ground during winter, which was followed by −12 to +8 mm/day (lower than mean scenario) during summer due to low precipitation and evaporation. Furthermore, the wet scenario (Figure 6c) is similar to the mean, with the exception that the summer is only five months (May through September).

The monthly cumulative flux under the mean scenario (Figure 6a) was initially 0 mm up to March because of frozen surface. It decreased to −5 mm by April, as snowmelt primarily resulted in runoff because infiltration through the soil pores was low. It remained constant in May despite more rain and evaporation, both of which occurred through the soil pores as well as cracks [23]. The flux peaked to +12 mm by June and remained positive in July because of frequent and high-intensity rain events. It gradually decreased to −10 mm by October because of low rainfall and remained constant thereafter because of frozen surface. The overall negative net flux (except for May to July) is attributed to the arid (Dfb) weather under the mean scenario. Under the dry scenario (Figure 6b), the flux decreased from 0 mm to −15 mm by January, remained constant till May, peaked to −2 mm by June, and gradually decreased to −20 mm by December. The initial decrease and the subsequent negative values up to May are attributed to the absence of snow cover, which increased evaporation. Under the wet scenario (Figure 6c), the flux remained zero till April because of snow cover. It rapidly increased to +50 mm by June due to high snowmelt and frequent and high-intensity rains. The flux gradually decreased to +30 mm by September and remained constant thereafter due to an early freezing condition at the surface.

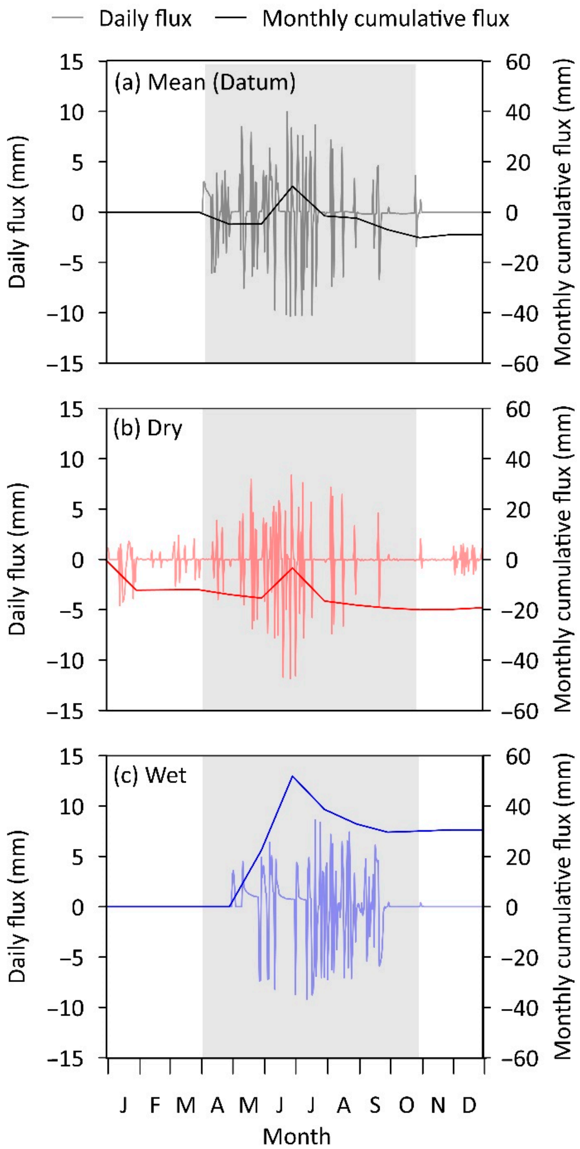

Figure 6. Predicted net water flux under the investigated scenarios: (**a**) mean (datum); (**b**) dry; and (**c**) wet.

Figure 7 gives the cumulative volume changes at selected depths for Stage-I indices over a one-year timeframe: + for heave, and – for settlement. The volume change on 1 January was set to zero to ensure direct comparison of the various indices. At 0.3 m depth (Figure 7a), the datum (black curve) showed minor variation of −5 mm from January to April due to snow cover and frozen ground. This was followed by a gradual settlement up to −17 mm by June due to the negative flux in April and May (Figure 6a). Thereafter, the soil showed gradual heave up to +2 mm by October due to positive flux in June and July. This delay in soil response is due to the low hydraulic conductivity of the soil (Figure 3b), which resulted in slow water movement. The soil continued to increase in heave up to +8 mm by December due to movement of existing water from before under a frozen surface. Such a cyclic trend of soil displacement was reported through 1961 and 1968 field monitoring data [50] and confirmed through numerical modeling using a suction-based approach [31] and seepage-based approach [23]. The deformations in the datum scenario gradually decreased with depth and diminished at 3.1 m below surface. This is because heave is cancelled by soil overburden [51] and settlement is subdued because soils cannot release water from deeper layers [52].

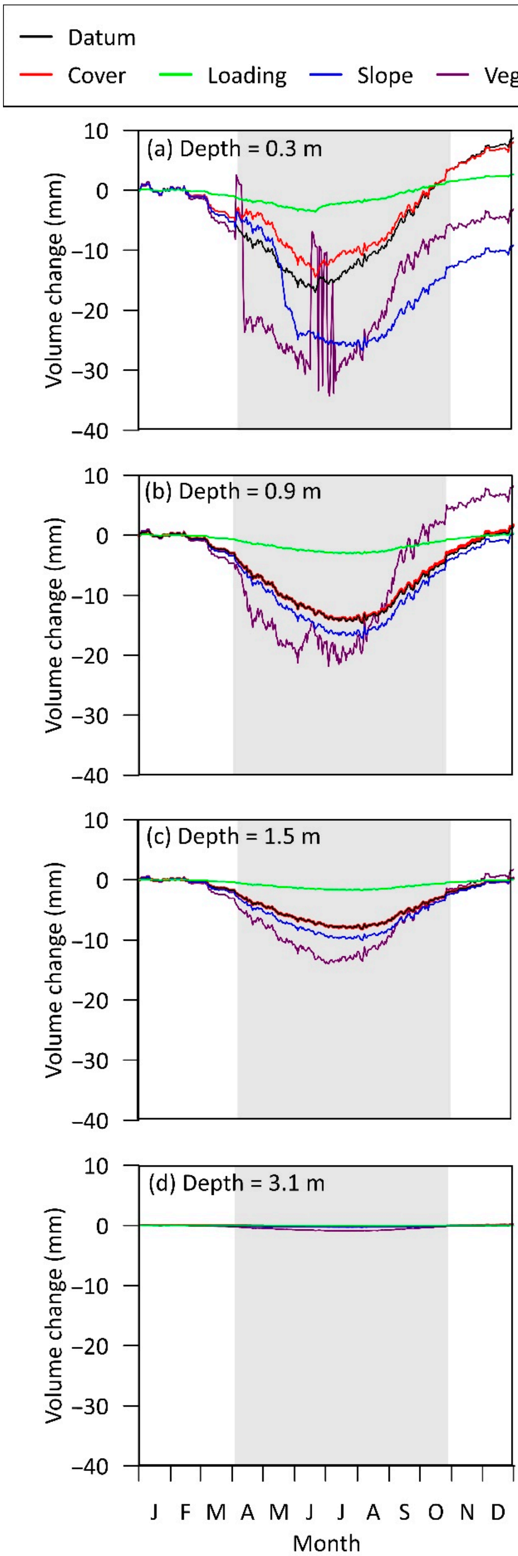

Figure 7. Transient volume changes at selected depths for Stage-I indices: (**a**) depth = 0.3 m; (**b**) depth = 0.9 m; (**c**) depth = 1.5 m; and (**d**) depth = 3.1 m.

For all Stage-I indices, the seasonal and depth (highest at 0.3 m) trends were identical, albeit with different magnitudes. Under cover, the displacement generally plotted 0 to −12 mm decreases (up to 5 mm above the datum curve) in early summer due to restricted evaporation in summer and −15 mm to +6 mm heave (up to 2 mm below the datum) in winter due to restricted infiltration. Under loading (300 kPa), soil settled up to −4 mm (end of June) and bounced back to +2 mm (end of December). This relatively lower volume change is attributed to a reduced void ratio of the soil under a structural load [53]. Under slope, the soil showed a minor volume change up to −5 mm by April followed by a rapid decrease to −25 mm by June and then by a gradual increase to −20 mm by December. The rapid initial decrease and the low bounce-back in volume change compared to the datum scenario is due to increased runoff, resulting in negligible water infiltration [54]. Under vegetation, the curve showed a rapid heave in early April from −8 mm to +3 mm, quick settlement (−25 mm) in May, cyclic deformations from −30 mm to −5 mm during June and July, and gradual increase to −8 mm by December. This trend is similar to the datum scenario, except for June and July. During these months, vegetation is active, thereby resulting in increased evapotranspiration through leaves and increased infiltration via the root system [55]. Among all Stage-I indices, volume change fluctuations were highest for vegetation index owing to enhanced evapotranspiration and infiltration, followed by slope index because of surface runoff, then by cover index due to isolation of soil from atmosphere, whereas loading index diminished most of the deformations.

Figure 8 gives the cumulative volume changes at various depths over a one-year timeframe for Stage-II indices: + for heave, and – for settlement. Results of the datum scenario are the same as in Figure 7. Under the dry scenario, the initial water content index at 0.3 m depth showed a significant drop to −30 mm compared with 0 mm at datum at the start of the simulated year owing to the imposed initial condition. Thereafter, an opposite trend to the datum (Figure 7) was observed with minor variations of −30 mm to −25 mm and back to −30 mm. This lower vertical displacement compared to the datum is attributed to the lateral consumption of swelling in the initially opened cracks [56]. As expected, the precipitation index was generally below the datum such that the minimum reached −30 mm by June and bounced back to −4 mm by December. The effect of precipitation was reported to be the most critical among the metrological parameters [57]. The remainder of the Stage-II indices followed the datum curve with some fluctuations. This means that air temperature, wind speed, relative humidity, and net radiation have minimal impact on soil volume change. With respect to depth, transient fluctuations gradually decreased for all other Stage-II indices. Under the wet scenario, the initial water content index at 0.3 m showed a significant heave of +40 mm compared with 0 mm at the datum at the start of the simulated year owing to the imposed initial condition. Thereafter, it linearly increased to +50 mm by June and then remained primarily constant because of surface ponding. As expected, the precipitation index showed 0 mm till April and continuously increased to +18 mm by December. The air temperature index did not significantly affect volume change because of frozen ground conditions for most of the year. The wind speed, relative humidity, and net radiation closely matched and showed identical trends as the datum scenario. With respect to depth, transient fluctuations were lower than the dry scenarios.

Figure 9 presents the risk evaluation vectors for selected infrastructure types using Stage-I indices. Deformations at 0.3 m were used for surface facilities, namely open areas (Figure 9a), roads (Figure 9b), and buildings (Figure 9c), whereas deformations at 1.5 m were used for underground pipes (Figure 9d). The datum scenario at surface showed no risk till February due to frozen soil, increased to 2.3 by June due to settlement arising from moisture deficit, diminished by October due to heaving arising from preceding summer rainfall, and rose to 1.0 by December due to heaving. A similar trend was observed for the datum scenario at 1.5 m depth, albeit with subdued risks, that is, up to 1.2 in summer-fall and negligible in winter. All of the urban infrastructure types showed the same seasonal patterns as their respective datum. In comparison to the datum, the risk was two times in parks, insignificant in roads, one-half in five story buildings, and one-fourth for pipes under roads. These changes are attributable to the assignment of overall weights based on expert judgement (Table 1).

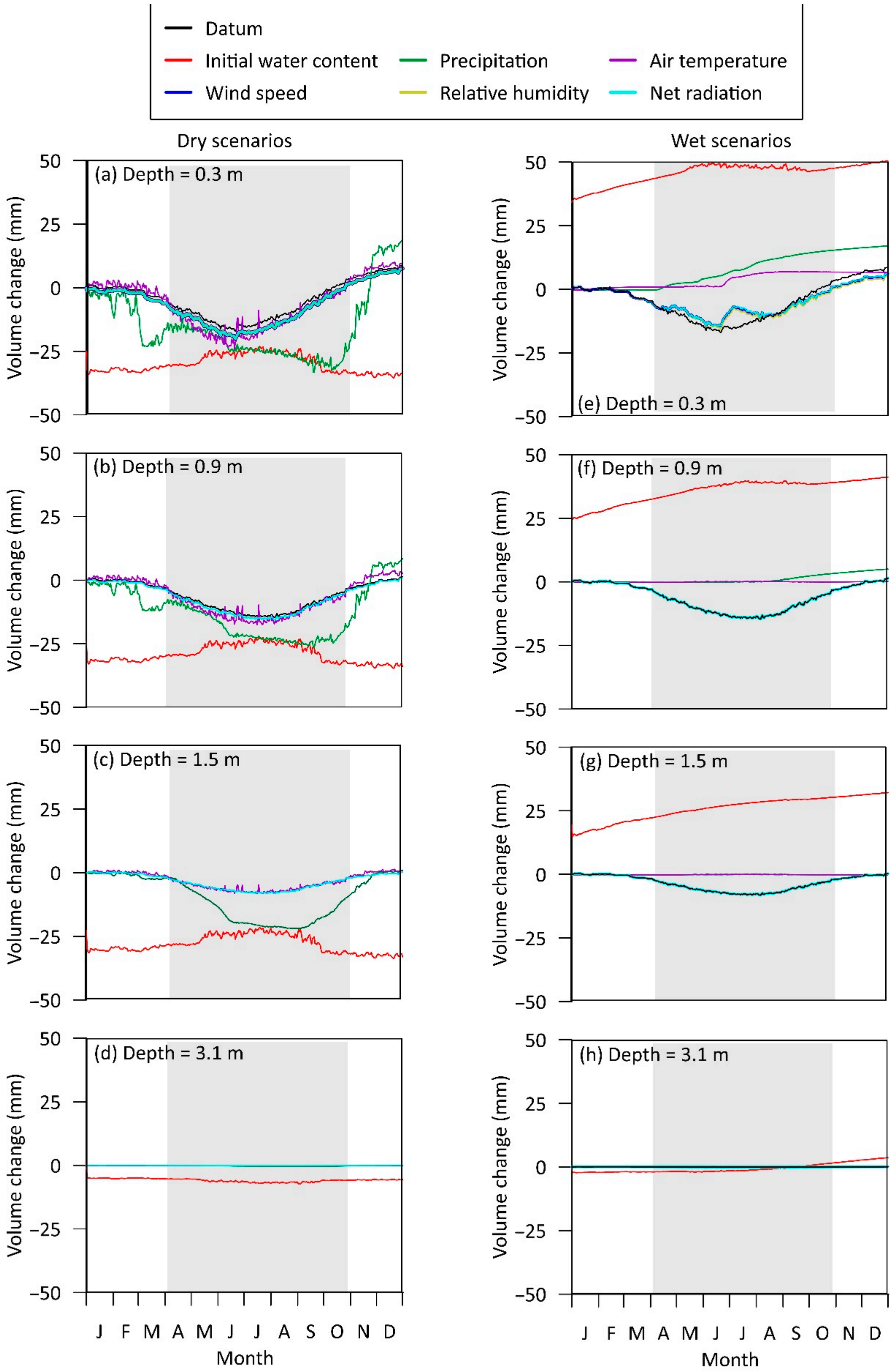

Figure 8. Transient volume changes at selected depths for Stage-II indices: (**a**) depth = 0.3 m; (**b**) depth = 0.9 m; (**c**) depth = 1.5 m; (**d**) depth = 3.1 m; (**e**) depth = 0.3 m; (**f**) depth = 0.9 m; (**g**) depth = 1.5 m; and (**h**) depth = 3.1 m.

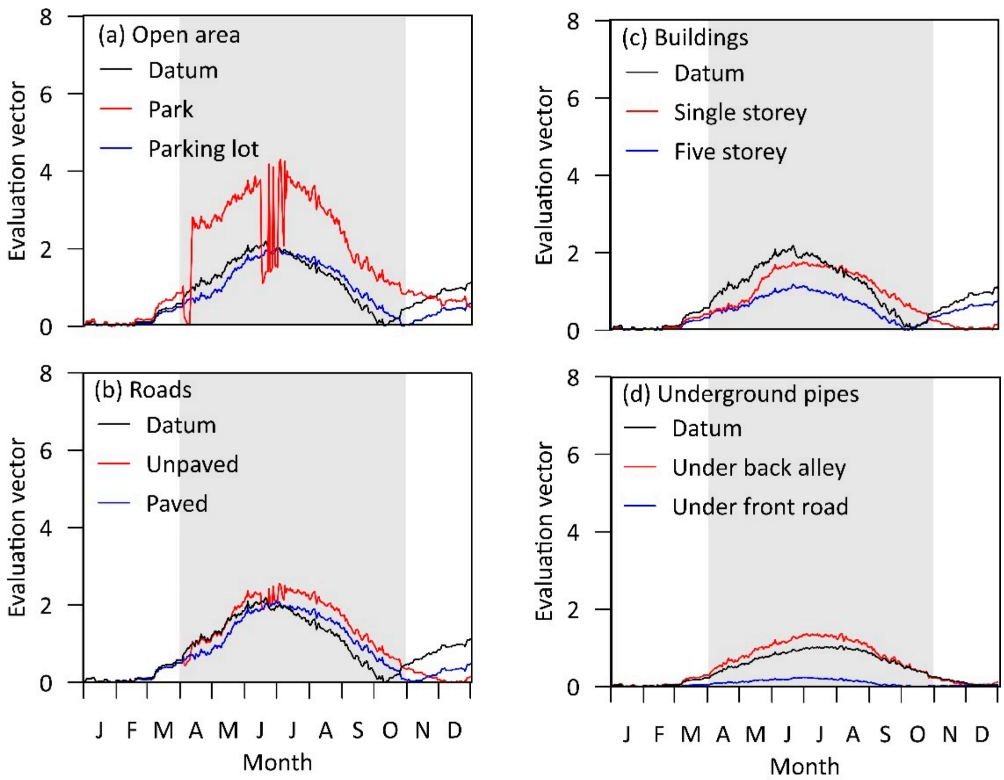

Figure 9. Transient variations in evaluation vectors for Stage-I indices: (**a**) open area; (**b**) roads; (**c**) buildings; and (**d**) underground pipes.

Figure 10 presents the risk evaluation vectors for Stage-II indices. Results of the datum scenario are the same as in Figure 9. As expected and based on Figure 8, the data indicate similar trends for all of the indices because of similar seasonal weather patterns. In comparison to the datum, the risk for the initial water content index inhibited seasonal variations, the precipitation index was about half with a wider distribution; all of the other indices showed about one-third the values. These departures are attributed to the product of high magnitudes and low $p = 0.025$ (high return period of 40 years) for both dry and wet conditions. To highlight the relative impact of extreme conditions, the probability of indices was increased to 0.129 while keeping the magnitude and the weight as before. This resulted in a high magnified risk for all of the indices such that the most critical were the initial water content and precipitation.

The limitations of this research are divided into three categories. The numerical model can be improved by capturing volume changes due to variations in freeze–thaw, snow melting, ground water table, crack depth, and daytime duration. Stage-I indices can include the following: spatial heterogeneity in the soil properties; human activity such as lawn watering, pipeline leakage, snow dumping, and house heating; surface conditions such as impermeable asphalt, vehicular load, slope orientation, and large trees; and non-linearity between the datum and the maximum values. Likewise, Stage-II indices can be improved by considering following: spatial variation in metrological parameters; effect of solar radiation, cloud thickness, and albedo on evaporation; interactions of atmospheric parameters to identify other long-term extreme weather conditions; and short-term extreme weather simulation such as high intensity storm, drought followed by rain fall, high snow melt followed by drought, and rain fall on snow dump.

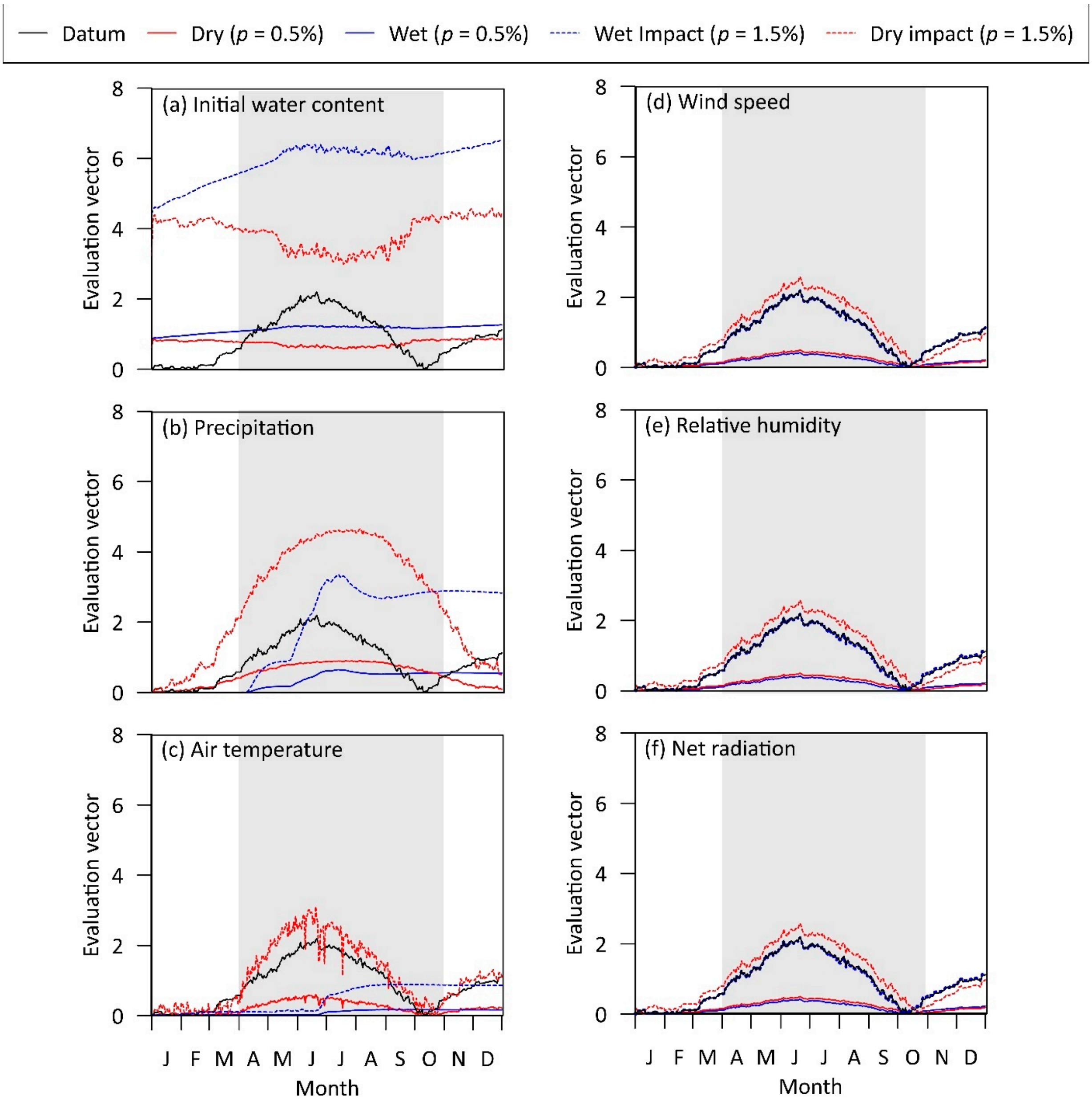

Figure 10. Transient variations in evaluation vectors and risk impacts under datum, dry, and wet scenarios for Stage-II indices: (**a**) initial water content; (**b**) precipitation; (**c**) air temperature; (**d**) wind speed; (**e**) relative humidity; and (**f**) net radiation.

6. Summary and Conclusions

Knowledge of surface- and weather-related volumetric changes are critical for civil infrastructure supported by expansive soils. The primary achievement of this research is the development of a numerical-hierarchical framework that captured surface conditions and climate parameters. Using numerically predicted transient volume changes, one datum scenario (exposed to mean weather), four surface scenarios (cover, loading, slope, and vegetation), two extreme antecedent moisture scenarios (dry and wet), and ten extreme meteorological parameter scenarios (dry and wet) were analyzed. The risk of volume change was hierarchically determined for eight types of infrastructure utilizing the four surface scenarios (Stage-I indices) based on expert judgement as well as for antecedent moisture and atmospheric parameter scenarios (Stage-II indices) using normal distribution functions. The main results of this research are summarized as follows:

Under the datum scenario, the soil surface exhibited minor variations up to −5 mm from January to April, a steady settlement up to −17 mm by June, and a gradual heave up to +8 mm by December. Such cyclic variations were found in all the Stage-I indices such that the fluctuations were highest for vegetation, followed by slope, then by cover, and lowest for loading. Volume changes gradually reduced with depth and diminished at 3.1 m.

Among the Stage-II indices, similar cyclic trends to the datum were generally obtained, except for initial water content (dry and wet), precipitation (dry and wet), and air temperature (wet). Volume change under dry initial water content dropped to −30 mm and showed an opposite trend with minor variations. In contrast, the same index under wet conditions showed a heave of +40 mm at the start and a linear increase to +50 mm by December.

Volume changes under dry precipitation were below the datum, reaching a minimum of −30 mm by June and bouncing back to −4 mm by December. When wet, the same index showed no volume change until April and continuously increased to +18 mm by December. Volume increase under wet air temperature was minor during most of the year. The transient seasonal fluctuations in volume change gradually decreased with depth for all Stage-II indices.

Under the datum scenario, risk was non-existent till February, increased to 2.3 by June, diminished by October, and rose back to 1.0 by December. Similar values for cyclic variations in risk were found in most urban facilities. Volume changes were found to be two times higher in parks, insignificant for roads, one-half for five-story buildings, and one-fourth for pipes under roads.

Among the Stage-II indices, the risk for the initial water content inhibited seasonal variations, the precipitation was about one-half with a wider distribution; all the other indices showed about one-third the values. When the probability was increased to 0.129, a magnified risk was observed for all the indices such that the most critical were the initial water content and precipitation.

Author Contributions: Data curation and analysis, Q.H.; Supervision, S.A.; Writing—original draft, Q.H.; Writing—review & editing, S.A. All authors have read and agreed to the published version of the manuscript.

Funding: This project was funded by the Natural Science and Engineering Research Council of Canada and SaskEnergy, Inc. through a collaborative research and development grant.

Institutional Review Board Statement: Not applicable.

Informed Consent Statement: Not applicable.

Data Availability Statement: The authors can provide access to modeling data upon request.

Acknowledgments: The authors thank the University of Regina for providing computational facilities.

Conflicts of Interest: The authors declare there are no conflict of interest.

References

1. Habibbeygi, F.; Nikraz, H.; Chegenizadeh, A. Intrinsic Compression Characteristics of an Expansive Clay from Western Australia. *Int. J. Geomate* **2017**, *12*, 140–147. [CrossRef]
2. Ito, M.; Azam, S. Relation between Flow through and Volumetric Changes in Natural Expansive Soils. *Eng. Geol.* **2020**, *279*, 105885. [CrossRef]
3. Zou, W.L.; Han, Z.; Ye, J. Bing Influence of External Stress and Initial Density on the Volumetric Behavior of an Expansive Clay during Wetting. *Environ. Earth Sci.* **2020**, *79*, 211. [CrossRef]
4. Chaduvula, U.; Viswanadham, B.V.S.; Kodikara, J. A Study on Desiccation Cracking Behavior of Polyester Fiber-Reinforced Expansive Clay. *Appl. Clay Sci.* **2017**, *142*, 163–172. [CrossRef]
5. Hakami, B.A.; Seif, E.S.S.A. Expansive Potentiality of Sabkha Soils of Rabigh Lagoon, Saudi Arabia: A Case Study. *Arab. J. Geosci.* **2019**, *12*, 107. [CrossRef]
6. Khan, M.S.; Hossain, S.; Ahmed, A.; Faysal, M. Investigation of a Shallow Slope Failure on Expansive Clay in Texas. *Eng. Geol.* **2017**, *219*, 118–129. [CrossRef]
7. Budhu, M. *Soil Mechanics Fundamentals*, 3rd ed.; John Wiley & Sons: Chichester, UK, 2015; ISBN 978-0-470-57795-0.

8. Shi, F.; Peng, X.; Liu, Z.; Li, E.; Hu, Y. A Data-Driven Approach for Pipe Deformation Prediction Based on Soil Properties and Weather Conditions. *Sustain. Cities Soc.* **2020**, *55*, 102012. [CrossRef]
9. Dafalla, M.A.; Shamrani, M.A. Road Damage Due to Expansive Soils: Survey of the Phenomenon and Measures for Improvement. In *GeoHunan International Conference 2011*; ASCE: Reston, VI, USA, 2011; pp. 73–80. [CrossRef]
10. Zumrawi, M.; Abdelmarouf, A.O.; Gameil, A. Damages of Buildings on Expansive Soils: Diagnosis and Avoidance. *Int. J. Multidiscip. Sci. Emerg. Res.* **2017**, *6*, 108–116.
11. Gallage, C.P.K.; Chan, D.; Kodikara, J. Response of a Plastic Pipe Buried in Expansive Clay. *Proc. Inst. Civ. Eng. Geotech. Eng.* **2012**, *165*, 45–57. [CrossRef]
12. *City of Regina PWI17-8 Residential Road Renewal Program Annual Report*; REGINA: Regina, SK, Canada, 2017. Available online: http://reginask.iqm2.com/Citizens/Detail_LegiFile.aspx?Frame=&MeetingID=2151&MediaPosition=&ID=1341&CssClass (accessed on 23 February 2023).
13. Osman, M.A.; Charlie, W.A. Engineering Properties of Expansive Soils in Sudan. In Proceedings of the 5th International Conference on Expansive Soils 1984, Institution of Engineers, Adelaide, Australia, 21–23 May 1984; pp. 311–315.
14. Li, J.; Cameron, D.A.; Ren, G. Case Study and Back Analysis of a Residential Building Damaged by Expansive Soils. *Comput. Geotech.* **2014**, *56*, 89–99. [CrossRef]
15. Jibson, R.W.; Harp, E.L.; Michael, J.A. A Method for Producing Digital Probabilistic Seismic Landslide Hazard Maps. *Eng. Geol.* **2000**, *58*, 271–289. [CrossRef]
16. Komac, M. A Landslide Susceptibility Model Using the Analytical Hierarchy Process Method and Multivariate Statistics in Perialpine Slovenia. *Geomorphology* **2006**, *74*, 17–28. [CrossRef]
17. Hasekioğulları, G.D.; Ercanoglu, M. A New Approach to Use AHP in Landslide Susceptibility Mapping: A Case Study at Yenice (Karabuk, NW Turkey). *Nat. Hazards* **2012**, *63*, 1157–1179. [CrossRef]
18. Yalcin, A. GIS-Based Landslide Susceptibility Mapping Using Analytical Hierarchy Process and Bivariate Statistics in Ardesen (Turkey): Comparisons of Results and Confirmations. *Catena* **2008**, *72*, 1–12. [CrossRef]
19. Thomas, P.J.; Baker, J.C.; Zelazny, L.W. An Expansive Soil Index for Predicting Shrink-Swell Potential. *Soil Sci. Soc. Am. J.* **2000**, *64*, 268–274. [CrossRef]
20. Look, B.G. Elements of Expansive Clay Roadway Specifications. *Aust. Geomech. J.* **2018**, *53*, 109–124.
21. Zhang, J.; He, P.; Xiao, J.; Xu, F. Risk Assessment Model of Expansive Soil Slope Stability Based on Fuzzy-AHP Method and Its Engineering Application. *Geomat. Nat. Hazards Risk* **2018**, *9*, 389–402. [CrossRef]
22. Saaty, T.L.; Katz, J.M. How to Make a Decision: The Analytic Hierarchy Process. *Eur. J. Oper. Res.* **1990**, *48*, 9–26. [CrossRef]
23. Huang, Q.; Azam, S. Modeling of Weather-Induced Volumetric Changes in Cracked Expansive Clays. *Geotech. Geol. Eng.* **2022**. [CrossRef]
24. Lyu, H.M.; Zhou, W.H.; Shen, S.L.; Zhou, A.N. Inundation Risk Assessment of Metro System Using AHP and TFN-AHP in Shenzhen. *Sustain. Cities Soc.* **2020**, *56*, 102103. [CrossRef]
25. Wang, M.; Chen, G. A Novel Coupling Model for Risk Analysis of Swell and Shrinkage of Expansive Soils. *Comput. Math. Appl.* **2011**, *62*, 2854–2861. [CrossRef]
26. Xu, J.; Liu, Y.; Ni, Y. Hierarchically Weighted Rough-Set Genetic Algorithm of Rock Slope Stability Analysis in the Freeze–Thaw Mountains. *Environ. Earth Sci.* **2019**, *78*, 227. [CrossRef]
27. *ISO Guide 73:2009*; ISO Guide ISO-Risk Management—Vocabulary. International Organization for Standardization: Geneva, Switzerland. Available online: https://www.iso.org/standard/44651.html (accessed on 7 December 2022).
28. Rosenblum, G.R.; Lapp, S.A. The Use of Risk Index Systems to Evaluate Risk. In *Risk Assessment in Setting National Priorities*; Springer: Berlin/Heidelberg, Germany, 1989; pp. 183–193. [CrossRef]
29. Xiong, Z.; Zhuang, Y.; Hu, Y.; Wang, S. Research on Risk Assessment Index System of Expressway. *IOP Conf. Ser. Earth Env. Sci* **2021**, *632*, 022056. [CrossRef]
30. Huang, Q.; Azam, S. Determination of Volumetric Changes in Cracked Expansive Clays. *Innov. Infrastruct. Solut.* **2020**, *5*, 1–11. [CrossRef]
31. Ito, M.; Azam, S.; Clifton, W. Suction-Based Model for Predicting Cyclic and Transient Volume Changes in Expansive Clays Using a Material Property Function. *Eng. Geol.* **2022**, *296*, 106491. [CrossRef]
32. Ito, M.; Azam, S. Engineering Properties of a Vertisolic Expansive Soil Deposit. *Eng. Geol.* **2013**, *152*, 10–16. [CrossRef]
33. Ito, M. Effect of Seasonal Climate on Volume Change Behaviour of Regina Clay. Master's Thesis, University of Regina, Regina, SK, Canada, 2009.
34. Ebrahimi-B, N.; Gitirana, G.F.N., Jr.; Fredlund, D.G.; Fredlund, M.D.; Samarasekera, L. A Lower Limit for the Water Permeability Coefficient. In Proceedings of the 57th Canadian Geotechnical Conference, Quebec City, QC, Canada, 24–27 October 2004; pp. 12–19.
35. Aboufoul, M.; Garcia, A. Factors Affecting Hydraulic Conductivity of Asphalt Mixture. *Mater. Struct./Mater. Constr.* **2017**, *50*, 116. [CrossRef]
36. City of Regina Standard Construction Specification SECTION 2325 Supply of Asphaltic Pavement. 2018. Available online: https://www.regina.ca/export/sites/Regina.ca/business-development/land-property-development/.galleries/pdfs/Construction-Specifications/Full-Depth-Reclamation.pdf (accessed on 23 February 2023).

37. Council of American Building Officials. *CABO ONE AND TWO FAMILY DWELLING CODE*, 5th ed.; The Council of American Building Officials: Falls Church, VA, USA, 1992.
38. GEO-SLOPE International Ltd. Land-Climate Interaction Hydraulic Modeling of a Soil Cover System Located in Northern Canada. 2015. Available online: http://downloads.geo-slope.com/geostudioresources/examples/9/0/VadoseW/Soil%20Cover%20Modeling%20-%20Hydraulic%20Response.pdf (accessed on 23 February 2023).
39. Akhter, A.; Azam, S. Flood-Drought Hazard Assessment for a Flat Clayey Deposit in the Canadian Prairies. *J. Environ. Inform. Lett.* **2019**, *1*, 8–19. [CrossRef]
40. City of Regina Standard Construction Specifications SECTION 2999 List of Roadway Standard Drawings. 2018. Available online: https://www.regina.ca/export/sites/Regina.ca/business-development/land-property-development/.galleries/pdfs/Construction-Specifications/Roadway-Standard-Drawings.pdf (accessed on 23 February 2023).
41. City of Regina Standard Construction Specifications SECTION 2120 Embankments. 2017. Available online: https://www.regina.ca/export/sites/Regina.ca/business-development/land-property-development/.galleries/pdfs/Construction-Specifications/Embankments.pdf (accessed on 23 February 2023).
42. Zhu, H.; Zhang, L.M. Field Investigation of Erosion Resistance of Common Grass Species for Soil Bioengineering in Hong Kong. *Acta Geotech.* **2016**, *11*, 1047–1059. [CrossRef]
43. City of Regina Design Standard-Transportation. Regina. 2022. Available online: https://www.regina.ca/export/sites/Regina.ca/business-development/land-property-development/.galleries/pdfs/Design-Standard-Transportation.pdf (accessed on 23 February 2023).
44. Coulbourne Consulting Chapter 3: Design Loads for Residential Buildings. In *Residential Structural Design Guide, Second Edition: A State-of-the-Art Engineering Resource for Light-Frame Homes, Apartments, and Townhouses*; U.S. Department of Housing and Urban Development Office of Policy Development and Research: Washington, DC, USA, 2017.
45. Simms, P.H.; Yanful, E.K. A Pore-Network Model for Hydromechanical Coupling in Unsaturated Compacted Clayey Soils. *Can. Geotech. J.* **2005**, *42*, 499–514. [CrossRef]
46. Ito, M.; Azam, S. Stochastic Modeling of Volume Changes in Expansive Soils. *Innov. Infrastruct. Solut.* **2018**, *3*, 45. [CrossRef]
47. Zhong, X.; Zhang, T.; Wang, K. Snow Density Climatology across the Former USSR. *Cryosphere* **2014**, *8*, 785–799. [CrossRef]
48. Wilson, G.W. Soil Evaporative Fluxes for Geotechnical Engineering Problems. Ph.D. Thesis, University of Saskatchewan, Saskatoon, SK, Canada, 1990.
49. *Sask Energy Field Soil Temperature, A Report Submitted to SaskEnergy*; REGINA: Regina, SK, Canada, 2004.
50. Hamilton, J.J. Effects of Environment on the Performance of Shallow Foundations. *Can. Geotech. J.* **1969**, *6*, 65–80. [CrossRef]
51. Yoshida, R.T.; Fredlund, D.G.; Hamilton, J.J. The Prediction of Total Heave on a Slab-on-Grade Floor on Regina Clay. *Can. Geotech. J.* **1983**, *20*, 69–81. [CrossRef]
52. Fredlund, D.G.; Rahardjo, H.; Fredlund, M.D. *Unsaturated Soil Mechanics in Engineering Practice*; John Wiley & Sons, Inc.: Hoboken, NJ, USA, 2012; ISBN 9781118133590.
53. Peng, X.; Dörner, J.; Zhao, Y.; Horn, R. Shrinkage Behaviour of Transiently- and Constantly-Loaded Soils and Its Consequences for Soil Moisture Release. *Eur. J. Soil Sci.* **2009**, *60*, 681–694. [CrossRef]
54. Zhang, W.; Zhu, X.; Ji, S.; Chen, C.; Zeng, H.; Zou, X.; Yang, B.; Jiang, X.; Liu, W. Soil Water Movement Differences Relating to Banana (Musa Nana Lour.) Plantation Regime. *Land Degrad. Dev.* **2022**, *33*, 1821–1835. [CrossRef]
55. Bartens, J.; Day, S.D.; Harris, J.R.; Dove, J.E.; Wynn, T.M. Can Urban Tree Roots Improve Infiltration through Compacted Subsoils for Stormwater Management? *J. Environ. Qual.* **2008**, *37*, 2048–2057. [CrossRef] [PubMed]
56. Azam, S.; Wilson, G.W. Volume Change Behavior of a Fissured Expansive Clay Containing Anhydrous Calcium Sulfate. In Proceedings of the Fourth International Conference on Unsaturated Soils, 2–6 April 2006, Carefree, AZ, USA; American Society of Civil Engineers: Reston, VA, USA; pp. 906–915.
57. Ito, M.; Hu, Y. Prediction of the Behaviour of Expansive Soils. In Proceedings of the 2011 Pan-Am CGS Geotechnical Conference, Toronto, ON, Canada, 2–6 October 2011.